Experimental study on dynamic mechanical properties of concrete under sulfate attack

Ruixue Liu[1], Xianbiao Mao[2], Bing Li[1], Yan Li[1] and
Lianying Zhang[1]*

[1]School of Civil Engineering, Xuzhou University of Technology, Xuzhou, Jiangsu, China, [2]State Key
Laboratory for Geomechanics & Deep Underground Engineering, China University of Mining and
Technology, Xuzhou, Jiangsu, China

Research on the dynamic mechanical properties of concrete under sulfate attack is the basis for the reasonable design and performance evaluation of anti-explosion and impact resistance in concrete structures under the erosion environment. In this study, the mechanical properties of concrete specimens subjected to sulfate attack under impact compression were measured using the split Hopkinson pressure bar (SHPB) test system. The basic mechanical properties (stress-strain curve, compressive strength, elastic modulus, peak strain) of concrete specimens subject to sulfate attack under high strain rate were obtained, and the variation laws of macroscopic failure characteristics and characteristics of energy dissipation of concrete specimens subject to sulfate attack with the loading strain rate were summarized. The results show that the compressive strength and elastic modulus of concrete specimens under different sulfate concentrations exhibit a significant strain rate effect. As the strain rate increases, the compressive strength and elastic modulus of concrete specimens gradually increase; compared with concrete free from sulfate attack, the compressive strength and elastic modulus of concrete subject to sulfate attack are more significantly influenced by strain rate. Overall, the peak strain of concrete increases with the increase of strain rate, but when the strain rate increases to a certain extent, the peak strain changes little. Under the same sulfate concentration, the macroscopic failure degree of concrete specimens increases obviously with the increase of strain rate. The dissipation energy of concrete subject to sulfate attack is more sensitive to the strain rate compared with concrete free from sulfate attack, and the increase of strain rate will obviously decrease the energy utilization rate of concrete subject to sulfate attack.

KEYWORDS

concrete, sulfate attack, strain rate, dynamic mechanical properties, characteristics of
energy dissipation

1 Introduction

The service life of China's coastal ports, cross-sea bridges and other large-scale concrete structures has been significantly reduced due to their long-term exposure to the harsh marine erosion environment. Durability is a very important factor for the service life of concrete structures (Verre, 2021). Among many erosion hazards, sulfate attack has become one of the primary environmental factors affecting structural durability. In the engineering project, damage caused by sulfate attack in concrete structure is extremely common.

At present, significant progress has been made in the experimental research on the mechanical properties of concrete under sulfate attack (Liang et al., 2022; Gan et al., 2021; Li, 2024; Zang et al., 2022; Cao et al., 2022). To investigate the effect of sulfate solution concentration and erosion time on the mechanical properties of concrete, Gao et al. (2010) and Feng et al. (2010) studied the influence of sulfate solution concentration and the number of wetting-drying cycles on the mechanical properties of concrete. The study obtained the attenuation laws of the elastic modulus and compressive strength of concrete, and summarized the triaxial compressive strength criterion of concrete under sulfate attack. In terms of the anti-corrosion performance of concrete with different mix proportions, Wang et al. (2020) analyzed the influence of basalt fiber content on the durability of concrete under sodium sulfate attack. The study found that the crack resistance of concrete in the early stage can be significantly improved by adding basalt fiber in an appropriate amount, and the corrosion resistance of the test block with the basalt fiber content of 0.1% was the best. Serag Faried et al. (2021) and He (2017) conducted a comparative study on the influence of different nano-materials and their dosages on the resistance of high-performance concrete to sulfate attack. Wang et al. (2021) explored the effect of polycarboxylic acid water reducer with different side chain lengths on the sulfate corrosion resistance of concrete. The findings revealed that PCE with the shortest side chain provides the most effective enhancement of sulfate corrosion resistance. Hong et al. (2018) investigated the corrosion resistance of subway concrete exposed to magnesium sulfate solution at different concentrations. It was concluded that the concrete with a water-binder ratio of 0.35 and fly ash content of 30% showed the best corrosion resistance. Regarding the influence of sulfate attack on the mechanical properties of concrete, Zhang et al. (2020) studied the influence of sulfate attack on the failure mode of concrete under the conditions of semi-immersion and full immersion. The results indicated that the failure mode of the shear surface of the corroded specimen was mainly in the form of aggregate tumbling, peeling and matrix extrusion and sliding near the shear surface under the conditions of full immersion, while under the semi-immersion, matrix cracking and dilatancy slip were dominant in the shear surface. Song et al. (2023), Wu et al. (2024), Wu et al. (2022), Wu et al. (2020) established a residual strength calculation model for concrete using ultrasonic methods, providing an economical and convenient calculation method for engineering applications.

The existing research focuses on the mechanical properties of concrete subjected to sulfate attack under static loading. However, some important civil or military protective concrete components in service are not only subject to static loading, but also bear various dynamic loads, such as vehicle load, wind load, earthquake action, wave and explosion impact. Therefore, these concrete components must have sufficient explosion resistance and seismic resistance. Some scholars have conducted preliminary research on the mechanical properties of concrete under the combined action of sulfate corrosion and impact load. Wei et al. (2023) Investigated the dynamic mechanical properties of corroded coral concrete. The results showed that Coral concrete exhibited great dynamic properties under chemical attacks and higher damping capacity under sulfate attack than that of other erosion. Demei et al. (2016) analyzed the flexural strength, relative dynamic elastic modulus under sulfate attack incorporating with dynamic flexural loading, and also analyzed the microstructure and atom ratio of attached specimens via SEM and EDS. Liu et al. (2020) analyzed the effects of erosion form and erosion age on the dynamic properties of concrete.

In summary, over the past few years, research on the mechanical properties of concrete under sulfate attack has primarily focused on static loading. Relatively few studies have addressed on the mechanical properties of concrete subjected to sulfate attack and impact loading. There is a lack of systematic research on the strain rate effect on dynamic mechanical properties of concrete under the erosion by different concentrations of sulfate. Moreover, there is currently limited research on the energy dissipation of eroded concrete under impact loads. The dynamic mechanical properties of concrete materials after sulfate erosion should be studied comprehensively.

Therefore, this paper conducts research on the mechanical properties and energy dissipation of sulfate eroded concrete under impact load, obtaining the correlation between strain rates and dynamic mechanical properties (stress-strain curve, compressive strength, elastic modulus and peak strain), as well as energy dissipation characteristics of concrete under different concentrations of sulfate attack. The research results can provide important reference for the establishment of damage evolution models and dynamic response calculations.

2 Specimen preparation and test method

2.1 Specimen preparation

The concrete specimens were prepared in accordance with the relevant provisions of the *Code for Construction of Concrete Structures* (Ministry of Housing and Urban-Rural Development of the People's Republic of China, 2011). The strength of concrete specimens was prepared in accordance with C60, with the continuous particle size of crushed stone ranging from 5–8 mm. The specimen preparation process was as follows: (1) According to Table 1, the coarse aggregate (stone), fine aggregate (sand) and cement were put into the mixer and mixed for about 1 min, then the water was added and mixed for 2 min, and then the water reducer was added and mixed for 1 min. (2) The mixed concrete was then placed into a cube mold with a size of $100 \times 100 \times 100$ mm and vibrated on the vibrating table; the surface of the test piece was smoothed and placed indoors at the room temperature; after 24 h, the specimen was demoulded. (3) The demoulded specimen was then placed into the standard curing room for 28 days (see Figure 1). (4) The specimen was processed into a cylindrical specimen with a standard size of $\Phi\ 74^* \ 37$ mm (see Figure 2), and the unevenness of the two end faces was kept within 0.02 mm to improve the test accuracy.

TABLE 1 Design parameters of concrete specimen mix ratio.

Water-cement ratio	Water/kg m^{-3}	Cement/kg m^{-3}	Standard sand/kg m^{-3}	Metaling/kg m^{-3}
0.32	145	453	740	1,112

FIGURE 1
Specimen curing.

FIGURE 2
Partial processed concrete specimens.

FIGURE 3
Sulfate attack test.

FIGURE 4
SHPB test system.

2.2 Test method

(1) Firstly, the sulfate erosion test was conducted on the specimens in accordance with the Test Method of *Sulfate Resistance of Cement Concrete (T0582-2020)* (Ministry of Transport of the People's Republic of China, 2020). The detailed experimental steps are as follows: The Na_2SO_4 solutions with concentrations of 0.0%, 3.0%, 6.0% and 9.0% were prepared; The concrete specimens were placed into Na_2SO_4 solutions with different concentrations, and test specimens were completely immersed. Subsequently, the erosion test on concrete specimens was conducted (see Figure 3).

(2) After the erosion of 270 days, the concrete specimen was taken out and subject to uniaxial impact compression tests (see Figure 4). The basic dynamic mechanical parameters were determined by the split Hopkinson pressure bar (SHPB) testing system (with a diameter of 74 mm) in the State Key Laboratory for Geomechanics and Deep Underground Engineering of China University of Mining and Technology. The impact pressure was divided into four levels of 0.3, 0.4, 0.5 and 0.6 MPa. Each level of the impact air pressure was repeated 3–4 times, and the impact load was changed by adjusting the external air pressure.
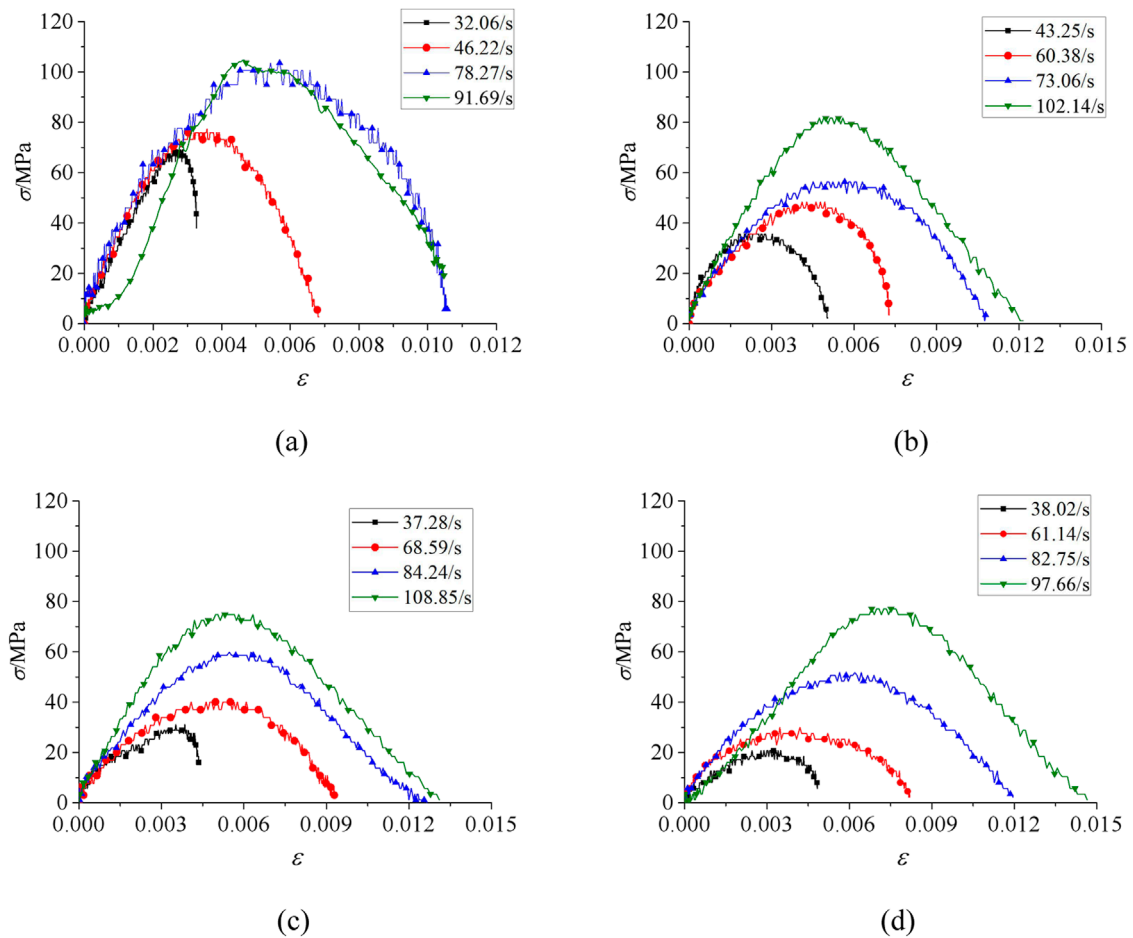
FIGURE 5
Variation law of stress–strain curve of concrete specimens with different stress rates. **(A)** $C = 0.0\%$ **(B)** $C = 3.0\%$. **(C)** $C = 6.0\%$ **(D)** $C = 9.0\%$.

Based on the uniaxial impact compression test data, the dynamic mechanical properties of concrete specimens subjected to sulfate erosion were obtained under different strain rates.

3 Strain rate effect on dynamic mechanical properties of concrete under sulfate attack

3.1 Variation law of stress-strain curve with strain rate

Based on the uniaxial compression test data of concrete specimens subject to sulfate attack under high strain rate, the change of stress-strain curve of concrete specimen with strain rate $\dot{\varepsilon}$ under impact load can be obtained, as shown in Figure 5.

As shown in Figure 5, the stress-strain curves of eroded specimens under high strain rates are essentially identical. The stress-strain curve can be divided into the following three stages: the approximate linear elastic stage, microcrack evolution and unstable propagation stage, and strain softening stage. In the first stage, the stress-strain curve is approximately linear, with continuous

accumulation of elastic energy. In the microcrack evolution and unstable propagation stage, the stress-strain curve presents an upward convex form; existing cracks in the specimen expand, new cracks form, and the stress reaches the maximum value at the end of this stage. In the strain softening stage, the stress decreases with the increase of strain, the bearing capacity of the concrete specimen decreases rapidly, and the concrete specimen undergoes rapid deformation.

By comparing the characteristics of the stress-strain curves of concrete specimens under different strain rates, it is evident that there are certain differences in the basic characteristics of the curves under different strain rates.

(1) As the strain rate $\dot{\varepsilon}$ increases, the peak stress σ_c of the specimens under different sulfate concentrations has the same variation law. Specifically, the peak stress increases gradually as the strain rate increases. Therefore, the peak stress is significantly influenced by the strain rate.

(2) As the strain rate $\dot{\varepsilon}$ increases, the slope of stress-strain curve rarely changes in the approximate linear elastic stage, indicating that the sensitivity of elastic modulus E of the specimen to strain rate $\dot{\varepsilon}$ is relatively low.
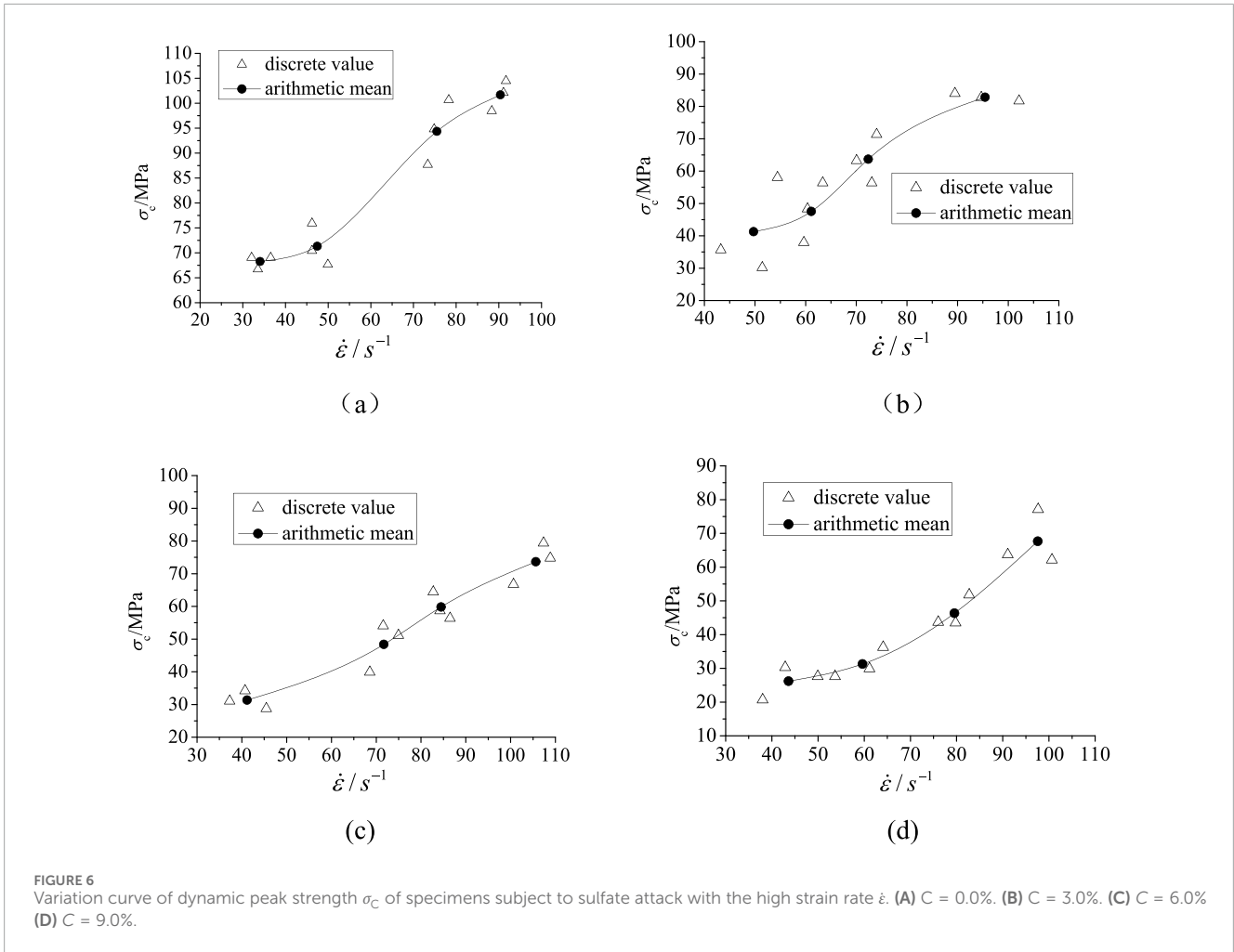
FIGURE 6
Variation curve of dynamic peak strength σ_C of specimens subject to sulfate attack with the high strain rate $\dot{\varepsilon}$. **(A)** C = 0.0%. **(B)** C = 3.0%. **(C)** C = 6.0%
(D) C = 9.0%.

(3) As the strain rate $\dot{\varepsilon}$ increases, the peak strain and the corresponding strain length during the strain softening process both increase gradually, indicating that the deformation degree of the specimen increases continuously. In fact, the increasing strain rate leads to the development of more cracks, resulting in the increase of internal defects and softening deformation after the peak.

3.2 Variation law of basic dynamic mechanical performance parameters with strain rate

Based on the stress-strain curve of the specimen under high strain rate, the variation of the specimen's compressive strength σ_c with the strain rate $\dot{\varepsilon}$ is analyzed. Figures 6, 7 show the variation curves of the compressive strength σ_c with the strain rate $\dot{\varepsilon}$ under different concentrations of sulfate attack. The average strain rate is the average value of the strain rates measured from several specimens under the same impact pressure.

As shown in Figure 6, with the increase of strain rate $\dot{\varepsilon}$, the strength σ_c of both non-eroded and eroded specimens gradually increases, showing obvious strain rate effect. Specifically, once
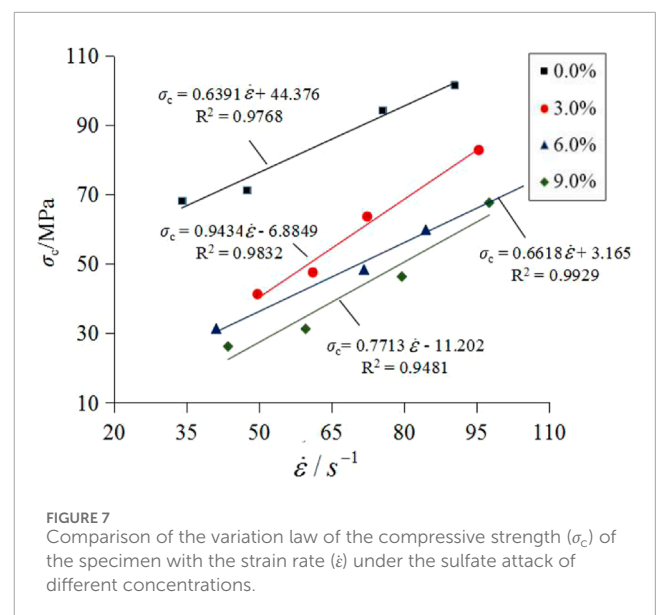

FIGURE 7
Comparison of the variation law of the compressive strength (σ_c) of the specimen with the strain rate ($\dot{\varepsilon}$) under the sulfate attack of different concentrations.

the strain rate exceeds a certain value, the compressive strength increases significantly with the increase of strain rate. The specific change process is as follows:

FIGURE 8
Variation curve of elastic modulus E of specimens subject to sulfate attack with the high strain rate $\dot{\varepsilon}$. **(A)** C = 0.0% **(B)** C = 3.0%. **(C)** C = 6.0% **(D)** C = 9.0%.

FIGURE 9
Comparison of the variation law of the elastic modulus E of the specimen with the strain rate $\dot{\varepsilon}$ under the sulfate erosion of different concentrations.
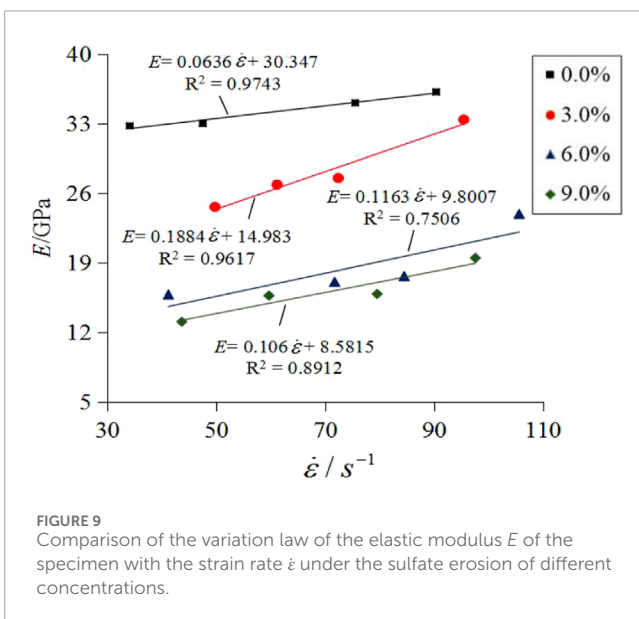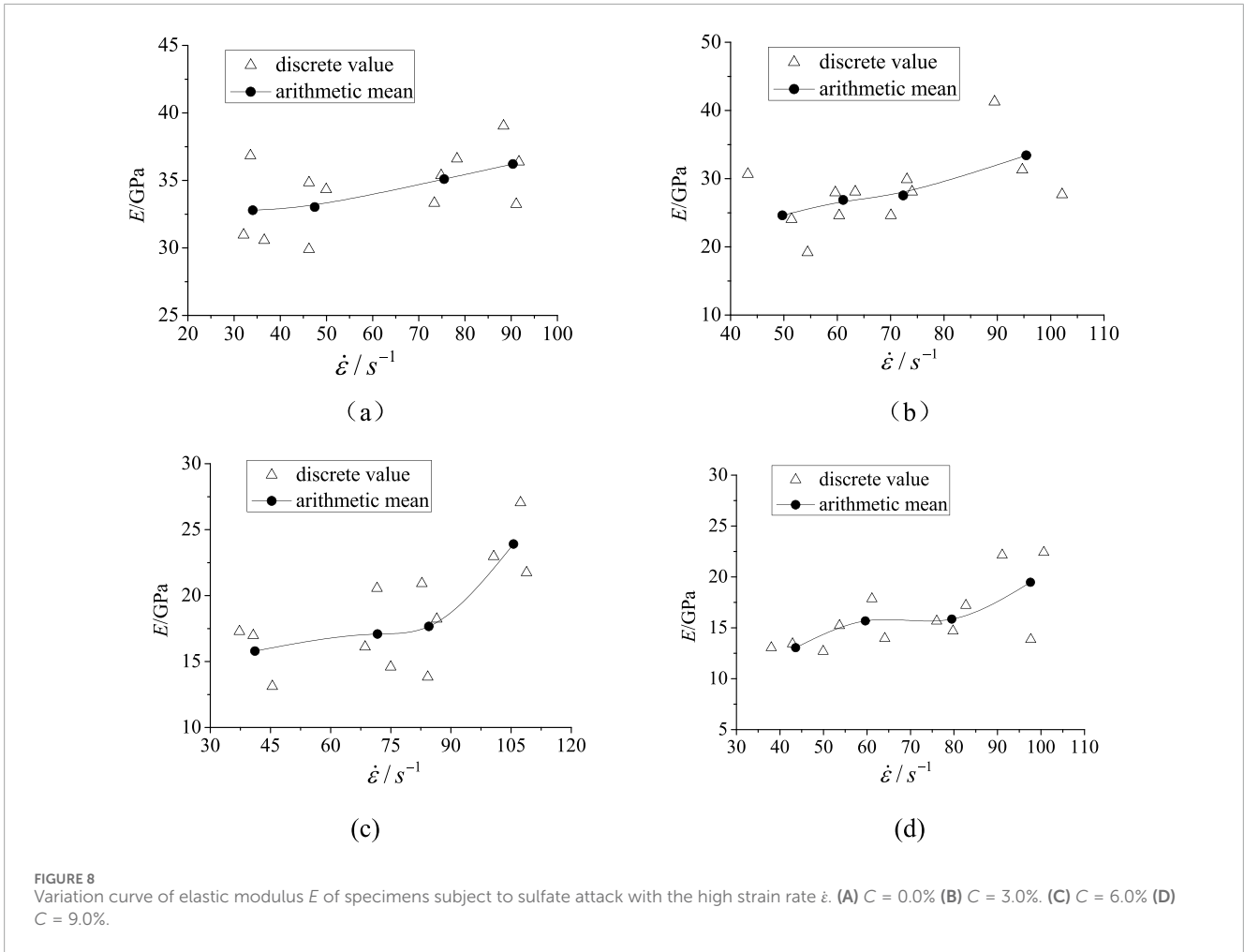
(1) When C = 0.0%, as the strain rate increases from 34.05/s to 90.38/s, the compressive strength of the specimen increases from 68.26 MPa to 101.67 MPa, with an increase of 48.95%; (2) When

C = 3.0%, as the strain rate increases from 49.71/s to 95.43/s, the compressive strength of the specimen increases from 41.28 MPa to 82.82 MPa, with an increase of 100.63%; (3) When C = 6.0%, as the strain rate increases from 41.16/s to 105.62/s, the compressive strength of the specimen increases from 31.34 MPa to 73.63 MPa, with an increase of 134.94%; (4) When C = 9.0%, as the strain rate increases from 43.62/s to 96.47/s, the compressive strength of the specimen increases from 26.21 MPa to 67.64 MPa, with an increase of 158.07%.

The compressive strength σ_c and strain rate $\dot{\varepsilon}$ of the specimens under sulfate attack of different concentrations were linearly fitted (see Figure 7). The slopes of the $\sigma_c - \dot{\varepsilon}$ linear equation for sulfate concentrations of 0.0%, 3.0%, 6.0% and 9.0% are 0.6391, 0.9434, 0.6618 and 0.7713, respectively. The slope of the linear equation of the eroded specimens is higher than that of the non-eroded specimens, which indicates that the strain rate effect on compressive strength of the eroded specimens is more obvious than that of the non-eroded specimens. However, due to the more significant effect of sulfate attack on the specimens' strength, the strength of the eroded specimens is still lower than that of the non-eroded specimens at high strain rates.

Based on the stress-strain curve of the eroded specimen under high strain rate, the variation of the elastic modulus E with the strain rate $\dot{\varepsilon}$ was analyzed. Figures 8, 9 show the variation curves of
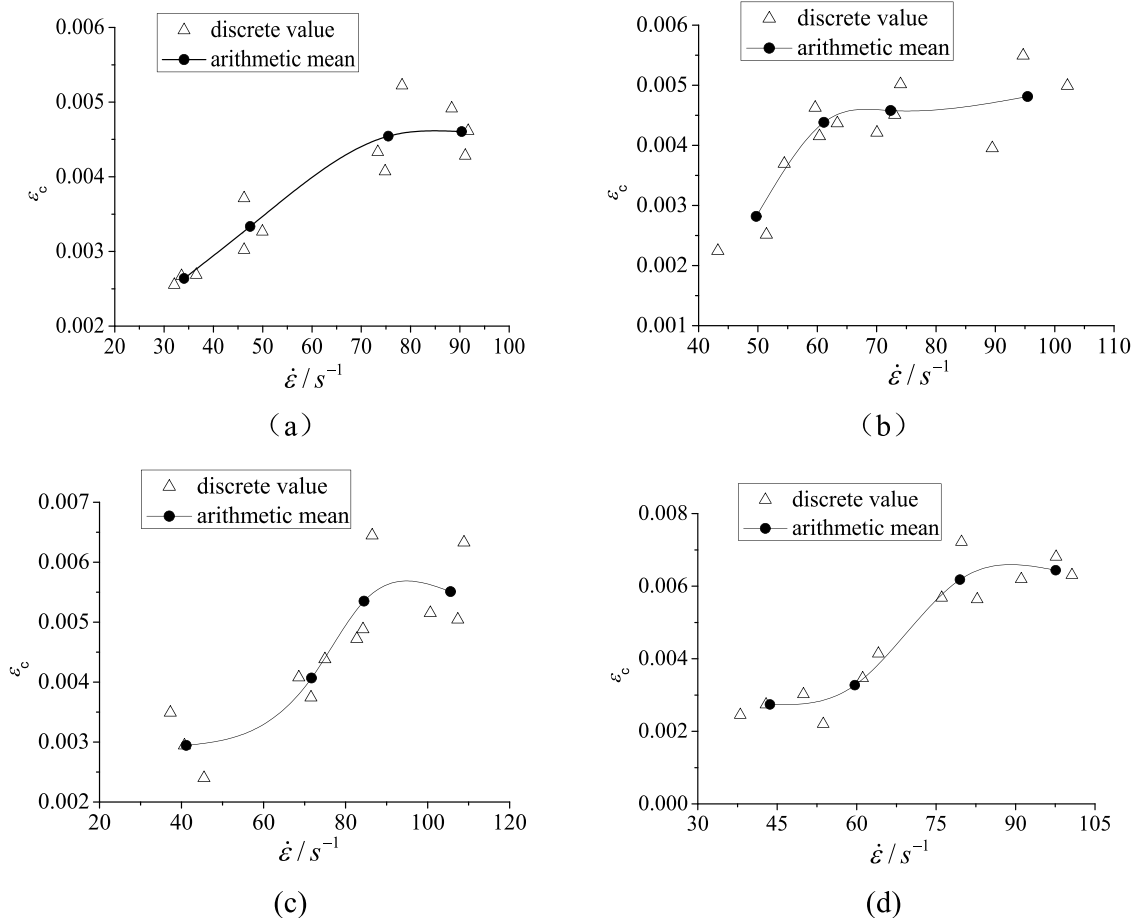
FIGURE 10
Variation curve of peak strain ε_c of specimens subject to sulfate attack with the high strain rate $\dot{\varepsilon}$. **(A)** $C = 0.0\%$ **(B)** $C = 3.0\%$. **(C)** $C = 6.0\%$ **(D)** $C = 9.0\%$.

specimens' elastic modulus E with the strain rate $\dot{\varepsilon}$ under different concentrations of sulfate attack.

As shown in Figure 8, with the increase of strain rate $\dot{\varepsilon}$, the elastic modulus E of the specimen gradually increases. The specific change process is as follows: (1) When $C = 0.0\%$, as the strain rate increases from 34.05/s to 90.38/s, the elastic modulus of the specimen increases slightly from 32.79 GPa to 36.21 GPa, with an increase of 10.43%; (2) When $C = 3.0\%$, as the strain rate increases from 49.71/s to 95.43/s, the elastic modulus of the specimen increases from 24.63 GPa to 33.41 GPa, with an increase of 35.65%; (3) When $C = 6.0\%$, as the strain rate increases from 41.16/s to 105.62/s, the elastic modulus of the specimen increases from 15.79 GPa to 23.92 GPa, with an increase of 51.49%; (4) When $C = 9.0\%$, as the strain rate increases from 43.62/s to 96.47/s, the elastic modulus of the specimen increases from 13.05 GPa to 19.47 GPa, with an increase of 49.20%.

With the increase of strain rate, the elastic modulus increases, indicating that the deformation resistance of the specimen gradually increases. In fact, at a higher strain rate, the lateral deformation in the middle of the specimen is limited due to the inertial effect. The higher the strain rate $\dot{\varepsilon}$, the greater the limiting effect. As a result, the deformation resistance of the specimen increases with the increase of the strain rate.

The elastic modulus E and strain rate $\dot{\varepsilon}$ of the specimens under sulfate attack of different concentrations are linearly fitted (see Figure 9). The slopes of E-$\dot{\varepsilon}$ linear equation of the specimen at the sulfate concentrations of 0.0%, 3.0%, 6.0% and 9.0% are 0.0636, 0.1884, 0.1163 and 0.1060, respectively. The slope of the linear equation of the eroded specimen is greater than that of the non-eroded specimens, indicating that the strain rate effect on the elastic modulus E of the eroded specimens is stronger than that of the non-eroded specimens. Since the elastic modulus of the eroded specimens decreases more significantly, under the higher strain rate, the elastic modulus of the eroded specimen is still lower than that of the non-eroded specimen.

Figures 10, 11 shows the variation of peak strain of concrete with strain rate $\dot{\varepsilon}$ under different concentrations of sulfate erosion.

Under different concentrations of sulfate erosion, the peak strain of the specimen shows a significant strain rate effect (see Figure 10). Overall, the peak strain of the specimen gradually increases with the increase of strain rate, and at higher strain rates, the slope of the change curve shows a decreasing trend. The specific change process is as follows: (1) When $C = 0.0\%$, as strain rate increases from 34.05/s to 90.38/s, the peak strain of the specimen increases from 0.002637 to 0.004604, with an increase of 74.59%; (2) When $C = 3.0\%$, as strain rate increases from 49.71/s to 95.43/s, the peak
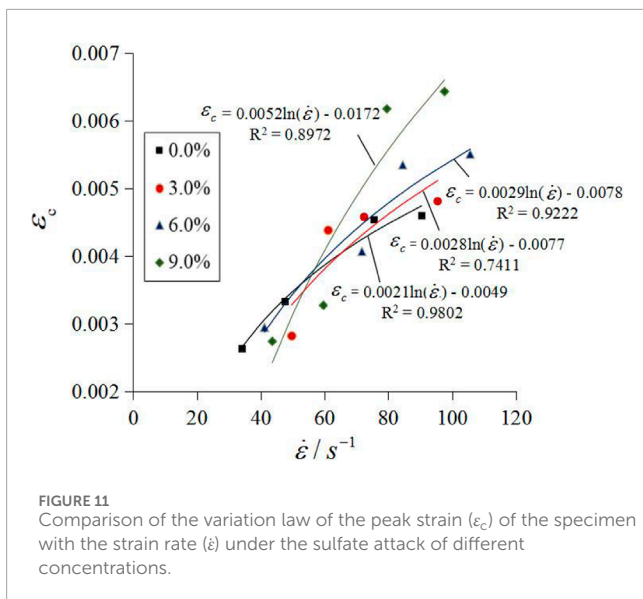
FIGURE 11
Comparison of the variation law of the peak strain (ε_c) of the specimen with the strain rate ($\dot{\varepsilon}$) under the sulfate attack of different concentrations.

strain of the specimen increases from 0.002818 to 0.004812, with an increase of 70.76%; (3) When C = 6.0%, as strain rate increases from 41.16/s to 105.62/s, the peak strain of the specimen increases from 0.002945 to 0.005509, with an increase of 87.06%; (4) When C = 9.0%, as strain rate increases from 43.62/s to 96.47/s, the peak strain of the specimen increases from 0.002738 to 0.006436, with an increase of 135.06%.

In fact, as the strain rate increases, the number of cracks generated increases, and the deformation of the specimen at the peak strength increases, resulting in an increase in peak strain. However, as the strain rate increases, the load application time shortens, leading to a shorter deformation time for specimen. Therefore, the combined effect of these two factors may cause the peak strain to increase more slowly with increasing strain rate at higher strain rates.

The logarithmic function provides a good fit for the relationship between the peak strain and strain rate of specimens under sulfate erosion (see Figure 11). The linear coefficients corresponding to concentrations of 0.0%, 3.0%, 6.0%, and 9.0% are 0.0021, 0.0028, 0.0029, and 0.0052, respectively. The strain rate effect on the peak strain of the specimens subjected to sulfate erosion at concentrations of 3.0% and 6.0% shows little change compared to the specimens without erosion. However, the strain rate effect on the peak strain of the eroded specimens at a concentration of 9.0% is significantly enhanced compared to the non-eroded specimens. This indicates that under erosion at a concentration of 9.0%, the effect of strain rate on the toughness of concrete is more significant.

3.3 The influence of strain rate on the macroscopic failure characteristics of specimens

Figures 12–15 show the failure modes of specimens subject to sulfate erosion under different loading strain rates $\dot{\varepsilon}$. The test results indicate that the tensile failure is the primary failure mode of the specimen under uniaxial impact compression. The change rule of

the failure mode of the specimen under different concentration of sulfate attack with the strain rate $\dot{\varepsilon}$ is similar, and the specific change rule is as follows:

(1) Under the same concentration of sulfate attack, the breakage degree of specimens increases with the increase of strain rate $\dot{\varepsilon}$. At a lower strain rate, cracks are generated from the periphery of the specimen, and the specimens are broken into several large blocks, with some fragments. The specimen cracks are large and run through the surface of the specimen. With the increase of the strain rate $\dot{\varepsilon}$, the crushing degree of the specimen is intensified, and the crushing area also continuously increases. Finally, the specimen is completely broken into small pieces under the high strain rate, and explosive failure occurs. The failure mode changes from axial failure to crushing failure.

(2) There are three fracture forms of concrete specimens under dynamic load: (1) the breaking of cement colloid, (2) the interface separation caused by the loss of adhesive force between cement and aggregate, and (3) the fracture of aggregate. These three fracture forms coexist in specimens under different strain rates in this study.

4 Energy dissipation characteristics of concrete under the high strain rate

Under the impact load, the concrete fracture caused by stress inevitably consumes a portion of the stress wave energy for crack propagation and the formation of new surface area (Shi et al., 2023; Shi et al., 2024). The energy consumption for crack propagation and new crack formation during concrete fragmentation is significantly different under different loading conditions. Therefore, to effectively crush or reinforce concrete, it is important to understand the differences in energy consumption for concrete crushing under various loading conditions.

4.1 Energy calculation principle of concrete under dynamic load

According to the test principle, the energy dissipation of concrete specimens during impact loading can be calculated through the input and output of energy in the pressure rod system. According to the elastic wave theory, the calculation functions for the incident energy W_I (J), reflected energy W_R (J), and transmitted energy W_T (J) in the SHPB experimental system are as shown in Equation 1.

$$\begin{cases} W_I = \dfrac{A_0 C_0}{E_0} \int_0^t \sigma_I^2(t)dt = A_0 C_0 E_0 \int_0^t \varepsilon_I^2(t)dt \\ W_R = \dfrac{A_0 C_0}{E_0} \int_0^t \sigma_R^2(t)dt = A_0 C_0 E_0 \int_0^t \varepsilon_R^2(t)dt \\ W_T = \dfrac{A_0 C_0}{E_0} \int_0^t \sigma_T^2(t)dt = A_0 C_0 E_0 \int_0^t \varepsilon_T^2(t)dt \end{cases} \quad (1)$$

Where W_I, W_R and W_T represent the incident energy, reflected energy, and transmitted energy in the system; A_0,
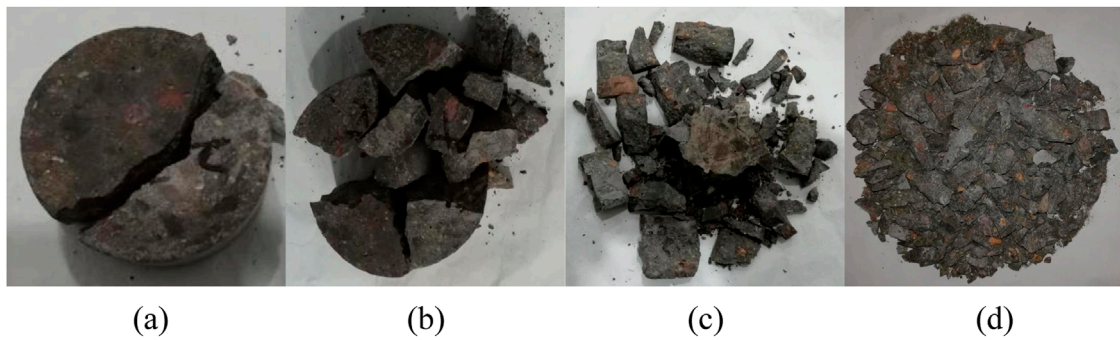
FIGURE 12
Macro failure mode of concrete specimens under different strain rates (*C* = 0.0%). **(A)** $\dot{\varepsilon}$ = 32.06/s **(B)** $\dot{\varepsilon}$ = 46.22/s **(C)** $\dot{\varepsilon}$ = 78.27/s **(D)** $\dot{\varepsilon}$ = 91.69/s.

FIGURE 13
Macro failure mode of concrete specimens under different strain rates (*C* = 3.0%). **(A)** $\dot{\varepsilon}$ = 43.25/s **(B)** $\dot{\varepsilon}$ = 60.38/s **(C)** $\dot{\varepsilon}$ = 73.06/s **(D)** $\dot{\varepsilon}$ = 102.14/s.
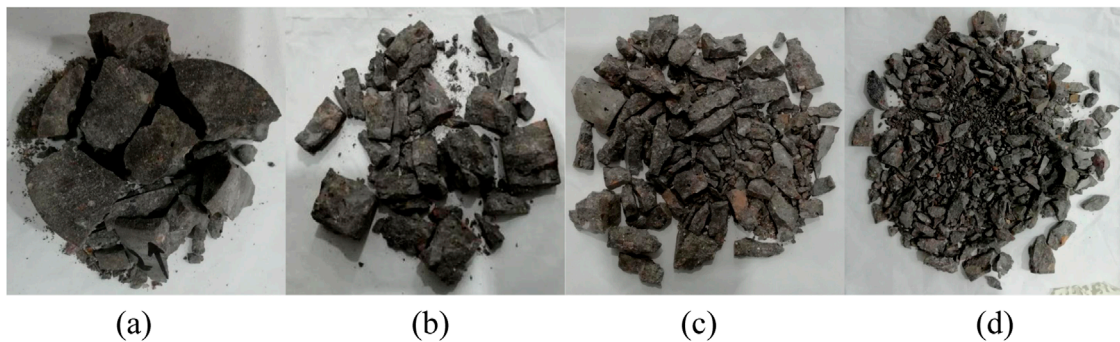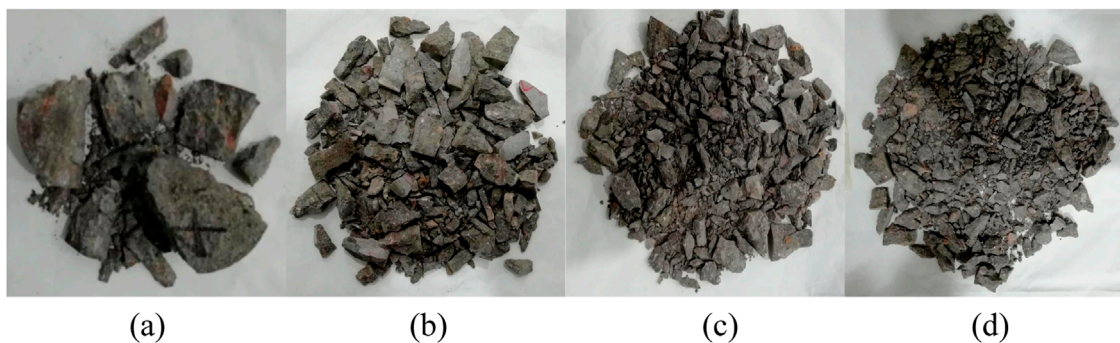

FIGURE 14
Macro failure mode of concrete specimens under different strain rates (*C* = 6.0%). **(A)** $\dot{\varepsilon}$ = 37.28/s **(B)** $\dot{\varepsilon}$ = 68.59/s **(C)** $\dot{\varepsilon}$ = 84.24/s **(D)** $\dot{\varepsilon}$ = 108.85/s.

C_0 and E_0 represent the cross-sectional area, (m^2), wave velocity (m/s), and elastic modulus of the compression rod (Pa); σ_I, σ_R and σ_T represent the stress (Pa) generated by incident waves, reflected waves, and transmitted waves in the compression rod.

Since butter is applied on the end face of the specimen to reduce the frictional effect, the frictional energy between the specimen and the compression rod can be ignored. Therefore, in the SHPB experiment, the absorbed energy W_L can be expressed as shown in Equation 2.

$$W_L = W_I - (W_R + W_T) = A_0 C_0 E_0 \int_0^t \{\varepsilon_I^2(t) - [\varepsilon_R^2(t) + \varepsilon_T^2(t)]\} dt \quad (2)$$

where W_L represents the absorbed energy (or dissipated energy) during specimen failure.

In the SHPB experiment, energy dissipation mainly includes the energy dissipation caused by specimen crack propagation (W_{LD}), fragment motion energy dissipation (W_{LV}), and other energy
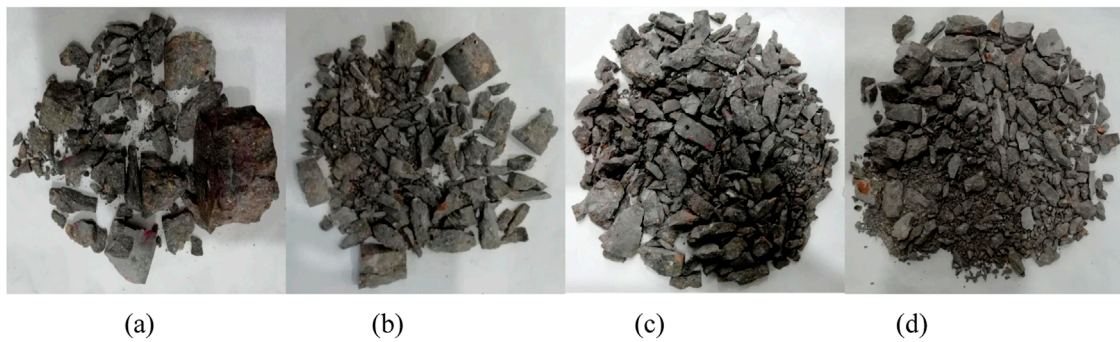
FIGURE 15
Macro failure mode of concrete specimens under different strain rates (C = 9.0%). **(A)** $\dot{\varepsilon}$ = 38.02/s **(B)** $\dot{\varepsilon}$ = 61.14/s **(C)** $\dot{\varepsilon}$ = 82.75/s **(D)** $\dot{\varepsilon}$ = 97.66/s.

dissipation (W_{LS}) such as frictional energy consumption. However, W_{LV} and W_{LS} account for a small proportion of W_L, and over 95% of the energy is used for crack propagation in the specimen. Therefore, it can be roughly assumed that $W_L \approx W_{Ld}$.

4.2 The effect of strain rate on energy dissipation of concrete under sulfate erosion

Based on the experimental results, the energy eigenvalues of non-eroded and eroded specimens (C = 9.0%, t = 270 days) under different strain rates were calculated (see Tables 2, 3). And standard deviations were also calculated, indicating that the experimental results are relatively stable.

Figure 16 shows the curves of energy W_J with strain rate of the non-eroded specimen. It can be seen from Figure 16 that with the increase of strain rate, the energies of non-eroded specimens show an increasing trend under impact loading. The change process is as follows: when the strain rate $\dot{\varepsilon}$ increases from 34.05/s to 90.38/s, the incident energy W_I increases from 56.64 J to 187.74 J (a 3-fold increase); the reflected energy W_R increases from 5.39 J to 54.39 J (a 10-fold increase); the transmitted energy W_T increases from 43.90 J to 111.58 J (a 2.54-fold increase); and the dissipated energy W_L increases from 7.34 J to 21.77 J (a 2.97-fold increase).

The fitting relationship between energy W_J and strain rate $\dot{\varepsilon}$ of non-eroded specimen is as shown in Equation 3.

$$\begin{cases} W_I = 25.532 e^{0.0222\dot{\varepsilon}} & R^2 = 0.9927 \\ W_R = 1.8089 e^{0.0377\dot{\varepsilon}} & R^2 = 0.9581 \\ W_T = 21.561 e^{0.0186\dot{\varepsilon}} & R^2 = 0.952 \\ W_L = 3.6095 e^{0.02\dot{\varepsilon}} & R^2 = 0.9947 \end{cases} \quad (3)$$

Figure 17 shows the curves of energy W_J with strain rate of the eroded specimen (C = 9.0%). It can be seen from Figure 17 that with the increase of strain rate, the energies of eroded specimens show an increasing trend under impact loading. The change process is as follows: when the strain rate increases from 43.62/s to 96.47/s, the incident energy W_I increases from 42.47 J to 181.78 J (a 8.35-fold increase); the reflected energy W_R increases from 13.12 J to 73.99 J (a 5.64-fold increase); the transmitted energy W_T increases from

3.13 J to 37.92 J (a 12.12-fold increase); and the dissipated energy W_L increased from 26.21 J to 69.88 J (a 2.67-fold increase).

The fitting relationship between energy W_J and strain rate of eroded specimen (C = 9.0%, t = 270 days) is as shown in Equation 4.

$$\begin{cases} W_I = 13.201 e^{0.0276\dot{\varepsilon}} & R^2 = 0.9949 \\ W_R = 3.5722 e^{0.0319\dot{\varepsilon}} & R^2 = 0.9841 \\ W_T = 0.3175 e^{0.0497\dot{\varepsilon}} & R^2 = 0.9805 \\ W_L = 12.069 e^{0.0198\dot{\varepsilon}} & R^2 = 0.9696 \end{cases} \quad (4)$$

The sensitivity of energy absorption capacity to strain rate $\dot{\varepsilon}$ before and after erosion is compared. Figure 18 shows the variation of dissipation energy W_{L0} and W_{LT} with strain rate $\dot{\varepsilon}$.

As shown in Figure 18, the dissipation energy W_L of both non-eroded and eroded specimens increases with the increase of strain rate. In fact, at high strain rates, the micro-structure inside the concrete (such as the inter-facial transition zone between cement paste and aggregate) is more susceptible to damage. Under high strain rate impact, micro-cracks rapidly propagate and form more fracture surfaces, thereby absorbing more energy and leading to an increase in dissipated energy. Moreover, the sensitivity of the dissipation energy W_{LT} of eroded specimens to strain rate is higher than that of non-eroded specimens W_{L0}. This phenomenon may be due to the loose deformation of the eroded specimen, and the dissipation energy W_L is more sensitive to the strain rate under impact loading.

At the same strain rate, a comparison of the dissipation energy W_L of non-eroded and eroded concrete specimens reveals that the energy absorption capacity of eroded specimens is obviously higher than that of non-eroded specimens. In fact, after being subjected to sulfate attack, the internal physical characteristics of concrete are altered, primarily due to changes in the internal joints and fractures. Under sulfate attack, some materials within the concrete, such as calcium hydroxide, undergo chemical reactions, leading to a loss of internal material volume and the formation of new joints and fractures. Meanwhile, the generated ettringite causes the joints and fractures to expand. The increase in the number of cracks, joints, and defect surfaces reduces the stability of the concrete, thereby diminishing its ability to resist damage. Under high strain rate, more cracks, joints, and defect surfaces are involved in the development and expansion of fractures.

TABLE 2 Energy calculation results of uniaxial impact compression of non-eroded specimens.

Specimen number	$\dot{\varepsilon}/s^{-1}$		W_I/J			W_R/J			W_T/J			W_L/J		
	Single specimen	Average	Single specimen	Average	Standard deviation	Single specimen	Average	Standard deviation	Single specimen	Average	Standard deviation	Single specimen	Average	Standard deviation
1	32.06	34.05	56.82	56.64	2.72	4.74	5.39	0.55	45.71	43.90	2.45	6.37	7.34	1.18
2	33.55		53.83			5.82			41.03			6.98		
3	36.53		59.26			5.61			44.96			8.69		
4	46.04	47.47	76.04	68.81	6.51	16.65	14.39	2.23	51.04	45.57	4.69	8.35	8.85	1.14
5	46.22		63.44			11.98			43.42			8.04		
6	50.14		66.95			14.53			42.26			10.16		
7	78.27	75.49	143.28	142.07	6.89	38.89	28.84	8.66	93.96	96.54	6.16	10.43	16.69	5.38
8	73.36		134.65			23.4			92.09			19.16		
9	74.85		148.28			24.22			103.58			20.48		
10	91.11	90.38	188.74	187.74	7.34	56.39	54.39	12	103.85	111.58	7.07	28.5	21.77	6.16
11	91.69		194.53			65.3			113.02			16.21		
12	88.34		179.96			41.49			117.87			20.6		

TABLE 3 Energy calculation results of uniaxial impact compression of eroded specimens (C = 9.0%, t = 270 days).

| Specimen number	$\dot{\varepsilon}/s^{-1}$		W_I/J			W_R/J			W_T/J			W_L/J		
	Single specimen	Average	Single specimen	Average	Standard deviation	Single specimen	Average	Standard deviation	Single specimen	Average	Standard deviation	Single specimen	Average	Standard deviation
1	38.02		35.33			8.61			3.95			22.78		
2	49.95	43.62	45.89	42.47	6.16	16.92	13.12	4.12	2.45	3.13	0.75	26.50	26.21	1.2
3	42.89		46.19			13.85			2.98			29.36		
4	53.68		58.88			21.91			2.75			34.22		
5	61.14	59.64	67.67	70.60	13.41	24.69	27.13	6.7	7.45	4.90	2.37	35.53	38.57	1.14
6	64.11		85.24			34.79			4.49			45.96		
7	76.05		122.59			42.03			16.64			63.93		
8	79.78	79.53	138.55	124.49	13.19	43.06	46.09	6.08	17.03	18.45	2.64	78.46	59.96	5.38
9	82.75		112.34			53.17			21.67			37.5		
10	97.66		192.49			90.88			41.19			60.43		
11	100.66	96.47	192.40	181.78	18.47	68.01	73.99	14.79	32.91	37.92	4.35	91.50	69.88	6.16
12	91.09		160.45			63.09			39.66			57.71		
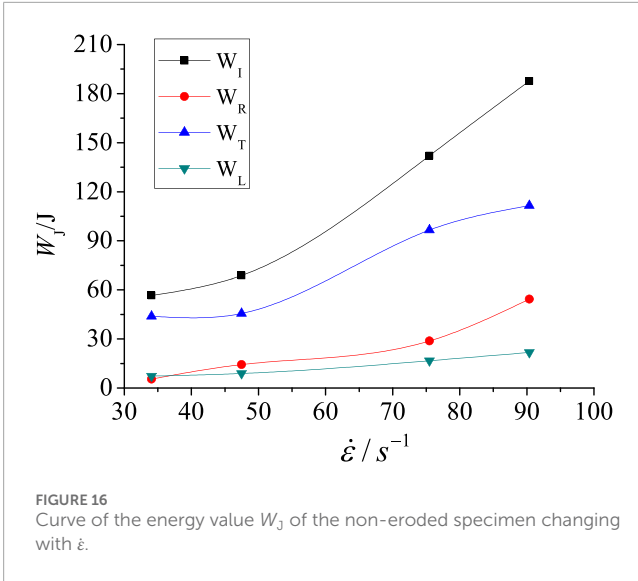
FIGURE 16
Curve of the energy value W_J of the non-eroded specimen changing with $\dot{\varepsilon}$.
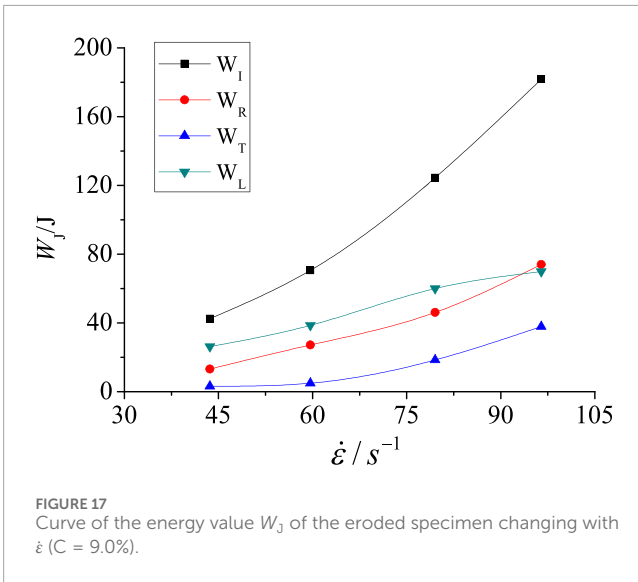

FIGURE 17
Curve of the energy value W_J of the eroded specimen changing with $\dot{\varepsilon}$ (C = 9.0%).
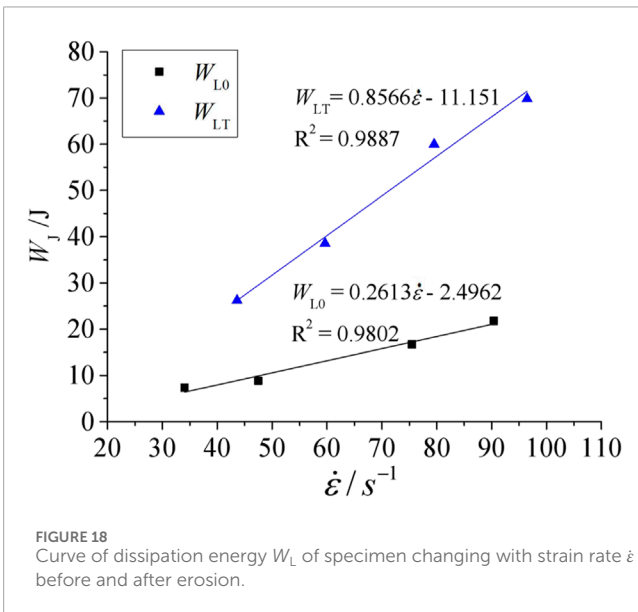

FIGURE 18
Curve of dissipation energy W_L of specimen changing with strain rate $\dot{\varepsilon}$ before and after erosion.
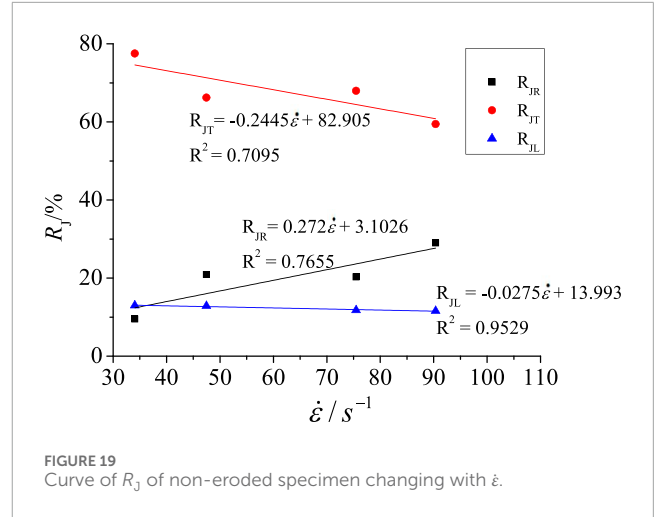

FIGURE 19
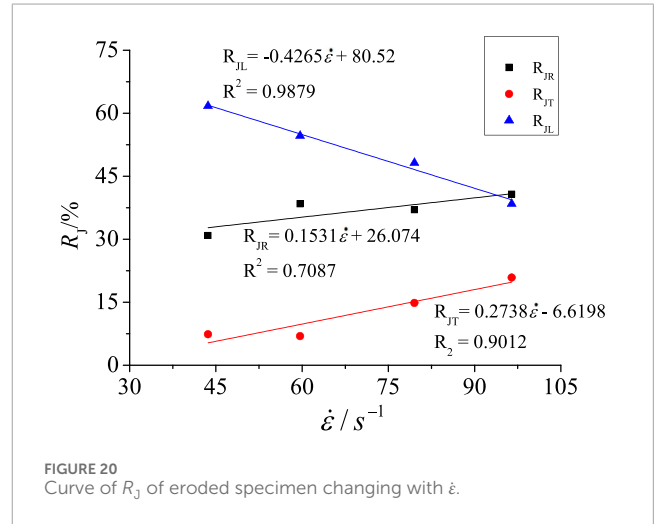Curve of R_J of non-eroded specimen changing with $\dot{\varepsilon}$.

FIGURE 20
Curve of R_J of eroded specimen changing with $\dot{\varepsilon}$.

This leads to an increase in the dissipated energy of the eroded concrete compared to the non-eroded concrete, enhancing its energy absorption capacity. Therefore, the macroscopic damage of the concrete under impact loading becomes more severe after erosion.

To further investigate the effect of strain rate on the energy utilization rate during the failure process of the specimen, the variation of the ratios of the reflected energy (W_R), transmitted energy (W_T) and the dissipation energy (W_L) to the incident energy (W_I) with the strain rate were studied. Figures 19, 20 show the ratios of these energies to incident energy (W_I) with strain rate for non-eroded and eroded specimens under impact loading.

As seen in Figure 19: the proportion of reflected energy to incident energy of the non-eroded specimen increases with the increase of strain rate, while the proportion of transmitted energy decreases with the increase of strain rate. The ratio of dissipation energy changes little with the increase of strain rate. The change process is as follows: when the strain rate increases from 34.05/s to 90.38/s, the proportion of reflected energy increases from 9.52% to 28.97%, with an increase of 204.43%; the proportion of transmitted

energy decreases from 77.51% to 59.43%, with an decrease of 23.32%; the proportion of dissipation energy decreases slightly from 12.97% to 11.59%, with an decrease of 10.61%.

As seen in Figure 20: with the increase of strain rate, the proportion of reflected energy and transmitted energy to incident energy of the eroded specimen (C = 9.0%, t = 270 days) increases, while the proportion of dissipation energy decreases. The change process is as follows: when the strain rate increases from 43.62/s to 96.47/s, the proportion of reflected energy increases from 30.90% to 40.70%, with an increase of 31.72%; the proportion of transmitted energy increases from 7.36% to 20.86%, with an increase of 183.35%; the proportion of dissipation energy decreases from 61.72% to 38.44%, with an decrease of 37.72%.

It indicates that the increase of strain rate will decrease the energy utilization ratio during the failure process of eroded concrete. The reason may be that the strength of the specimen decreases greatly and the structure becomes loose under the effect of sulfate attack. When the strain rate is high, the specimen can not absorb enough energy before it is destroyed. Moreover, the extent of increase of dissipation energy with the strain rate is less than that of the incident energy. Therefore, the ratio of dissipation energy decreases with the increase of strain rate.

5 Conclusion

In this study, the Split Hopkinson pressure bar (SHPB) test system was used to conduct the uniaxial impact compression test of concrete specimens under sulfate attack. The variation laws of the stress-strain curve, compressive strength, elastic modulus, characteristics of energy dissipation and macroscopic failure characteristics of concrete under different concentrations of sulfate attack with strain rate were analyzed. The research results can provide important reference for the establishment of damage evolution models and dynamic response calculations which are the basis for reasonable design of building structures and the evaluation of the blast and impact resistance performance of concrete structures in existing marine erosion environments. The main conclusions are as follows:

(1) The compressive strength and elastic modulus of concrete under different concentrations of sulfate show a certain strain rate effect. As the strain rate increases, both the compressive strength and elastic modulus of concrete gradually increase. The strain rate effect on the compressive strength and elastic modulus of eroded concrete is stronger than that of the non-eroded concrete. Overall, the peak strain of concrete gradually increases with the increase of strain rate, but after exceeding a certain strain rate, the change in peak strain becomes less significant.

(2) Under the same concentration of sulfate attack, with the increase of strain rate, the fragmentation degree of specimens increases, and the crushing area also expands. Finally, the concrete is completely broken into small pieces under

high strain rate, leading to a explosive failure of the concrete specimen.

(3) As the strain rate increases, the incident energy, reflected energy, transmitted energy, and dissipated energy of the specimen all show an increasing trend; the dissipated energy of the eroded specimen is more sensitive to the strain rate, however an increase of strain rate will significantly reduce the energy utilization efficiency during the failure process of the eroded specimen.

Data availability statement

The raw data supporting the conclusions of this article will be made available by the authors, without undue reservation.

Author contributions

RL: Writing–original draft. XM: Conceptualization, Writing–review and editing. BL: Writing–review and editing, Data curation. YL: Writing–review and editing. LZ: Writing–review and editing.

Funding

Conflict of interest

The authors declare that the research was conducted in the absence of any commercial or financial relationships that could be construed as a potential conflict of interest.

Generative AI statement

The authors declare that no Generative AI was used in the creation of this manuscript.

Publisher's note

All claims expressed in this article are solely those of the authors and do not necessarily represent those of their affiliated organizations, or those of the publisher, the editors and the reviewers. Any product that may be evaluated in this article, or claim that may be made by its manufacturer, is not guaranteed or endorsed by the publisher.

References

Cao, J., Han, Z., and Du, Z. (2022). Creep properties of axially compressed fly ash concrete under sulfate corrosion. *Adv. Mater. Sci. Eng.* 1 (1), 1–8. doi:10.1155/2022/6307740

Demei, Y., Bowen, G., He, R., Xiong, R., and Liu, Z. (2016). Sulfate attack of Portland cement concrete under dynamic flexural loading: a coupling function. *Constr. and Build. Mater.* 115, 478–485. doi:10.1016/j.conbuildmat.2016.02.052

Feng, Z., Liu, X., and Shucai, L. (2010). Study on triaxial strength criterion of concrete after seawater erosion. *Eng. Mech.* 27 (9), 209–210. doi:10.6040/j.issn.1672-3961.0.2022.240

Gan, L., Wu, J., Shen, Z., and Xianwei, F. (2021). Deterioration law of basalt fiber reinforced concrete under sulfate attack and dry-wet cycle. *China Civ. Eng. J.* 54 (11), 37–46. doi:10.19936/j.cnki.2096-8000.20230228.010

Gao, R., Shunbo, Z., Qingbin, L., and Chen, J. (2010). Experimental study of the deterioration mechanism of concrete under sulfate attack in wet-dry cycles. *China Civ. Eng. J.* 43 (2), 48–54.

He, J. (2017). *Study on sulfate resistance of nano-concrete foundation*. Harbin, Heilongjiang, China: Journal of Northeast Forestry University.

Hong, Q., Lucheng, X., and Hui, G. C. (2018). Experiment on durability of metro-concrete under action of double factors of sulfate and magnesium-salt. *J. Lanzhou Univ. Technol.* 44 (5), 144–149. doi:10.3969/j.issn.1673-5196.2018.05.026

Li, C. (2024). Study on compressive strength and sulfate corrosion resistance of limestone powder and waste glass powder mixed concrete. *Mater. Res. Express* 11 (2), 025502. doi:10.1088/2053-1591/ad1ef6

Liang, X., Cheng, H., Ma, Z., and Guan, B. (2022). Effects of manufactured sand lithology and gradation on sulfate resistance of concrete. *Bull. Chin. Ceram. Soc.* 41 (06), 1974–1980. doi:10.1007/s11595-014-1070-9

Liu, P., Chen, Y., Yu, Z., Lu, Z., and Shi, W. (2020). Evolution of the dynamic properties of concrete in a sulfate environment. *Constr. Build. Mater.* 245, 118468. doi:10.1016/j.conbuildmat.2020.118468

Ministry of Housing and Urban-Rural Development of the People's Republic of China (2011). *Code for construction of concrete structures: gb 50666-2011*. Beijing: China Architecture and Building Press.

Ministry of Transport of the People's Republic of China (2020). *Test method for sulfate resistance of cement concrete (T0582-2020)*. Beijing: People's Communications Press.

Serag Faried, A., Mostafa, S. A., Tayehc, B. A., and Tawfikd, T. A. (2021). Mechanical and durability properties of ultra-high performance concrete incorporated with various nano waste materials under different curing conditions. *J. Build. Eng.* 43, 102569. doi:10.1016/j.jobe.2021.102569

Shi, H., Chen, W., Zhang, H., Song, L., Ming, L., Wang, M., et al. (2023). Dynamic strength characteristics of fractured rock mass. *Eng. Fract. Mech.* 292, 109678. doi:10.1016/j.engfracmech.2023.109678

Shi, H., Zhang, H., Chen, W., Song, L., and Li, M. (2024). Pull-out debonding characteristics of rockbolt with prefabricated cracks in rock: a numerical study based on particle flow code. *Comput. Part. Mech.* 11 (1), 29–53. doi:10.1007/s40571-023-00607-9

Song, H., Fan, S., Zhang, S., and Gong, M. (2023). Strength deterioration prediction of pervious concrete in sulfate and dry-wet cycle environments utilizing ultrasonic velocity. *PLoS One* 18 (6), e0286948. doi:10.1371/journal.pone.0286948

Verre, S. (2021). Effect of different environments' conditioning on the debonding phenomenon in fiber-reinforced cementitious matrix-concrete joints. *Materialsy* 14 (24), 7566. doi:10.3390/ma14247566

Wang, C., Kong, F., and Pan, L. (2021). Effects of polycarboxylate superplasticizers with different side-chain lengths on the resistance of concrete to chloride penetration and sulfate attack. *J. Build. Eng.* 43, 102817. doi:10.1016/j.jobe.2021.102817

Wang, Z., Zong, M., Kai, Z., Zhe, L., and Jianbo, T. (2020). Experimental study on corrosion resistance and mechanical properties of basalt fiber concrete in sodium sulfate environment. *Build. Struct.* 20, 118–123. doi:10.19701/j.jzjg.2020.20.019

Wei, J., Cheng, B., Li, L., Long, W. J., and Khayat, K. H. (2023). Prediction of dynamic mechanical behaviors of coral concrete under different corrosive environments and its enhancement mechanism. *J. Build. Eng.* 63, 105507. doi:10.1016/j.jobe.2022.105507

Wu, J. Y., Jing, H. W., Gao, Y., Meng, Q. B., Yin, Q., and Du, Y. (2022). Effects of carbon nanotube dosage and aggregate size distribution on mechanical property and microstructure of cemented rockfill. *Cem. Concr. Compos.* 127, 104408. doi:10.1016/j.cemconcomp.2022.104408

Wu, J. Y., Jing, H. W., Yin, Q., Yu, L. Y., Meng, B., and Li, S. C. (2020). Strength prediction model considering material, ultrasonic and stress of cemented waste rock backfill for recycling gangue. *J. Clean. Prod.* 276, 123189. doi:10.1016/j.jclepro.2020.123189

Wu, J. Y., Wong, H. S., Zhang, H., Yin, Q., Jing, H. W., and Ma, D. (2024). Improvement of cemented rockfill by premixing low-alkalinity activator and fly ash for recycling gangue and partially replacing cement. *Cem. Concr. Compos.* 145, 105345. doi:10.1016/j.cemconcomp.2023.105345

Zang, X., Wang, G., Zhang, Z., Duan, X., and Hu, X. (2022). Study on mechanical behavior of reinforced concrete beams under sulfate attack. *Adv. Civ. Eng.* 1 (1). doi:10.1155/2022/3465281

Zhang, Z., Zhou, J., Zou, Y., Yang, J., and Jin, X. (2020). Effect of sulfate attack on the shear performance of concrete. *China Civ. Eng. J.* 53 (7), 64–72. doi:10.15951/j.tmgcxb.2020.07.005